Structural behaviour of asymptotic geodesic hybrid timber gridshells

Zongshuai Wan [a], Pierluigi D'Acunto [b], Eike Schling [a,c,*]

[a] *The University of Hong Kong, Department of Architecture, Hong Kong, China*
[b] *Technical University of Munich, School of Engineering and Design, Munich, Germany*
[c] *Leibniz University Hannover, Faculty of Architecture and Landscape Sciences, Hannover, Germany*

A B S T R A C T

Asymptotic geodesic gridshells are a novel structural system that is fabricated from straight and flat planks. The planks are elastically bent and twisted around their slender dimension to achieve the desired geometry, while the tall dimension creates structural stiffness. This system combines the geometric features of asymptotic and geodesic curves to create a hybrid tri-hex network on doubly curved surfaces, and provides a stable grid to resist its self-weight and external loads. To comprehensively explore the structural capabilities of asymptotic geodesic gridshells, a full-scale timber gridshell prototype was designed and built. Loading tests, including local and one shell asymmetrical loading, were carried out to examine the structural behaviour of the gridshell. A nonlinear finite-element model was developed and subsequently validated using experimental data. The evaluation of the timber gridshell revealed its high performance under uniformly distributed loads, and the simulation indicated a viable live load capacity of 7.0 kN/m^2. In a parametric study, the influence of the polar array layout, the joint rotation stiffness, and the support condition on the structural performance of the hybrid gridshell are analysed. Parameters influencing the achievable span are discussed regarding strength, stiffness and buckling behaviour for future design considerations.

1. Introduction

Gridshells employ their geometric curvature to achieve rigidity and resist external forces. They are often designed to span large areas with spatially curved shapes while minimizing material consumption. However, due to the complex nature of these geometries, the construction of gridshells often results in costly fabrication and assembly. The emerging field of "*construction-aware design*" [1] addresses this issue through an integrated design approach that combines architectural geometry, structure, and construction. By manipulating the design shape, novel construction techniques can be developed, facilitating the prefabrication of repetitive components or joints [2,3], and harnessing the advantages of form-active design.

Elastic gridshells offer a possible strategy to simplify fabrication, as they use the material's flexibility to create doubly curved shapes from flat and straight components. Frei Otto is credited with designing and constructing the Multihalle Mannheim [4], the world's first and largest elastic gridshell structure. This pioneering design uses the elastic deformation of square-section straight wood members to create a grid structure with a freeform inverted hanging shape. Since then, only a few

elastic reticulated shell structures have been built worldwide [5], such as the Weald and Downland Gridshell [6] and the Savill Garden Gridshell [7]. Typically, a form-finding process is required to determine a structure's shape, considering the significant torsion and bending deformations that occur during construction [8]. This process involves physical modeling and computational methods. *Architectural Geometry* has introduced a novel approach for designing networks by controlling the curvature of curves on surfaces [9]. Two specific approaches, *geodesic structures*, and *asymptotic structures*, offer the use of flat planks with beneficial properties for fabrication, assembly, and structural performance.

Geodesic structures have been explored for their construction simplicity and structural performance [10]. Natterer et al. [11] developed timber gridshells using flat geodesic planks and employed a layering technique to construct customized ribbed shells. Further studies in architectural geometry have examined adaptable geodesic patterns [12] and their ability to transform from flat to curved grids [13].

The mechanical advantages of asymptotic networks were first outlined in mathematical theory by Finsterwalder in 1897 [14]. Recent geometrical publications have investigated their developable properties

---

[15] and their discrete optimization as quad meshes [16]. The architectural potential of asymptotic structures to create deep gridshells from straight lamellas has been implemented in academia and practice. The first asymptotic gridshell was constructed from pairs of parallel steel lamellas with diagonal bracing [17]. A modular canopy design was prefabricated from single-welded steel with rigid edge beams and a membrane cover [18]. Another steel prototype explored the application potential as a façade module, investigating different panelization options [19].

Both geodesic and asymptotic constructions benefit from the elastic shaping of lamellas around their weak axis. However, the planks' slenderness also has negative effects on the structure's stability. For geodesic gridshells, the flat orientation of the lamella reduces the overall stability of the gridshell due to its lower stiffness in the out-of-plane direction. This issue is typically resolved by incorporating additional layers of planks [5]. In contrast, asymptotic gridshells exhibit greater global stability due to the vertical orientation of their lamellas [20]. However, slender lamellas may experience local compression buckling or lateral-torsional buckling [21]. To enhance the structural performance, the strategy of introducing couplings between two parallel asymptotic lamellas to form a double-lamella composite component has been explored [22].

Recently, a novel gridshell system has emerged, which stabilizes the lamella structure through the integration of asymptotic (A) and geodesic (G) curves, resulting in a triangulated hybrid AAG web [23]. The geodesic elements brace the asymptotic grid, creating a stable gridshell structure. This hybrid structure can be fabricated from straight, flat timber planks and elastically bent and twisted into a doubly curved surface shape, forming a rigid gridshell. In 2022, an Asymptotic Geodesic Hybrid Timber Gridshell prototype was designed and constructed in Munich, demonstrating the viability of the hybrid AAG system [24].

This paper delves into the structural behavior of the proposed asymptotic geodesic hybrid gridshells, based on experimental and numerical tests. We present new insights into the hybrid load-bearing behavior of flat and upright lamellas within this negatively curved gridshell. Specific construction parameters, such as *polar array layout*, *joint stiffness*, and *support condition*, are examined to better understand the structural performance and guide future development. Lastly, the scalability of the novel gridshell is systematically assessed to expand its application within the architectural field.

The paper is organized as follows. Section 2 introduces the related geometrical concepts (Section 2.1), describes the design and the construction of the asymptotic geodesic timber gridshell (Section 2.2) and outlines the loading setup for the physical loading tests (Section 2.3). Section 3 details finite element modelling for an overall prototype (Section 3.1) and a typical AA-joint (Section 3.2), respectively. Sections 3.3 and 3.4 discuss the supports and residual stresses. In Section 4, we compare experimental and numerical results under local area loading (Section 4.1) and one shell asymmetric loading (Section 4.2). The experimental data is utilized to validate the finite element model and analyse the structural behaviour of the hybrid timber gridshell. Section 5 employs the validated model to discuss the structural behaviour of the timber prototype under full-span uniformly distributed load (Section 5.1), and investigates the structural impact of polar array layout (Section 5.2), joint stiffness (Section 5.3), support condition (Section 5.4). Section 6 evaluates the potential to cover larger spans.

2. Physical prototype and testing setup

The design process of the AAG gridshell included a discrete optimization of the mesh geometry to satisfy geometric constrains like repetitive joints, straight planks, and geodesic boundary conditions. The construction process was accompanied by digital simulation of the structural behaviour using FE simulation, wind analysis and material testing to fulfil the Eurocode [24]. This paper focuses on the physical

testing of the prototype and a newly refined FE model, that precisely captures the load-bearing behaviour. In this section, we shortly introduce the geometric design of the prototypical structures, and discuss the physical loading test configuration, which was the basis for this refined FE model (Section 3) and its validation (Section 4).

2.1. Related geometry knowledge

Our research is deeply ingrained in the interdisciplinary field of *Architectural Geometry*, which merges insights from Design, Fabrication, Structural Engineering, and Mathematics. Specifically, we utilize theories from *Differential Geometry* to define a local coordinate system – the *Darboux Frame* (Fig. 1a) – in relation to the surface normal and curve tangent at any point along a curve on a surface. Three curvatures of curves are defined concerning the three axes of this Darboux Frame. The Geodesic Torsion τ_g represents the twist of the curve along its tangent. The Geodesic Curvature k_g is measured around the surface normal, while the normal curvature k_n measures the rotation of any curve around the local binormal, which is the cross product of the tangent and normal vector. By identifying paths on which k_g or k_n remain zero, we create networks that can be constructed exclusively from straight planks. As shown in Fig. 1, the mechanical bending directions - strong y, and weak z axes of a plank member can be specifically arranged along the geodesic and asymptotic curves. In this way, a network of geodesic curves (k_g=0) can be constructed from tangential planks (Fig. 1b). A network of asymptotic curves (k_n=0) can be built from upright planks (Fig. 1c), creating a deep quadrilateral grid. Asymptotic networks are of particular interest to us as they only exist on surfaces with negative Gaussian curvature, yet offer surprising benefits during construction. The geometric constraints enable the use of simple, off-the-shelf planks and repetitive joints for constructing highly complex gridshells. The upright lamellas are well-suited to resist external loads while allowing for an elastic erection process in which the grid is assembled flat and subsequently deformed (bent and twisted) into the desired doubly curved shape. During this process, the grid transforms predictably without the need for formwork, simplifying and reducing the cost of prefabrication. By adding geodesic planks for triangulation, we create rigid modules from standardized elements, which can be reused in a circular building economy. The potential of AAG gridshells for modular prefabrication is currently being developed in collaboration with an industry partner.

2.2. Specimen design and construction

2.2.1. Design

The Asymptotic Geodesic Hybrid Timber Gridshell [24] design is based on three symmetric AAG webs, which are polar-arrayed and combined to create a point-symmetric, negatively curved gridshell, as illustrated in Fig. 2. The geometry of the web was optimized numerically to ensure the asymptotic and geodesic properties with concentric intersection points, but also to create constant 60° intersection angles between asymptotic curves, as well as geodesic boundaries on two sides and bottom of the grid. These geometric features enabled the use of straight, flat wooden planks throughout the construction and the identical manufacturing of all joints. The reader is referred to [24] for more details on the design and optimization.

2.2.2. Timber construction

The structure is fabricated using 12×100 mm finger-jointed ash wood planks. These planks are pre-cut, drilled, and assembled in three layers. Asymptotic beams are created from two parallel planks each, coupled with 24 mm timber blocks. The two families of asymptotic beams are assembled on separate levels to enable continuous use of planks. Geodesic elements, constructed from single planks, are assembled as an intermittent layer connecting both the top and bottom asymptotic beams. The completed prototype is depicted in Fig. 3.
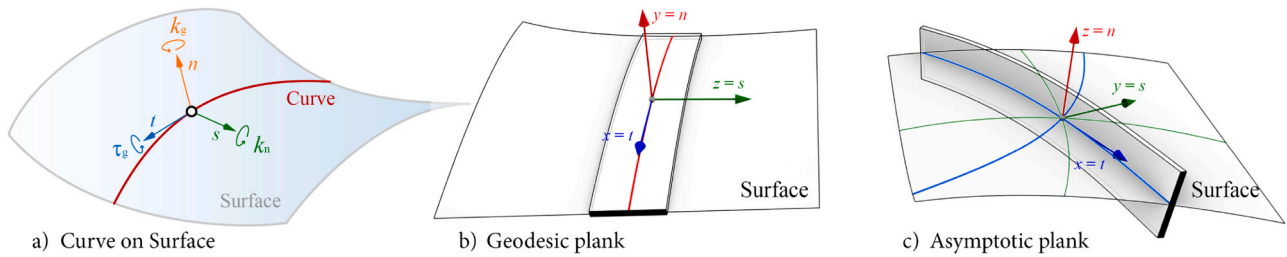
Fig. 1. Curvatures of a curve on a surface depicted using Darboux Frame (a), and their correspondence to the axes *x, y, z* of the geodesic plank (b) and asymptotic plank (c) [24].
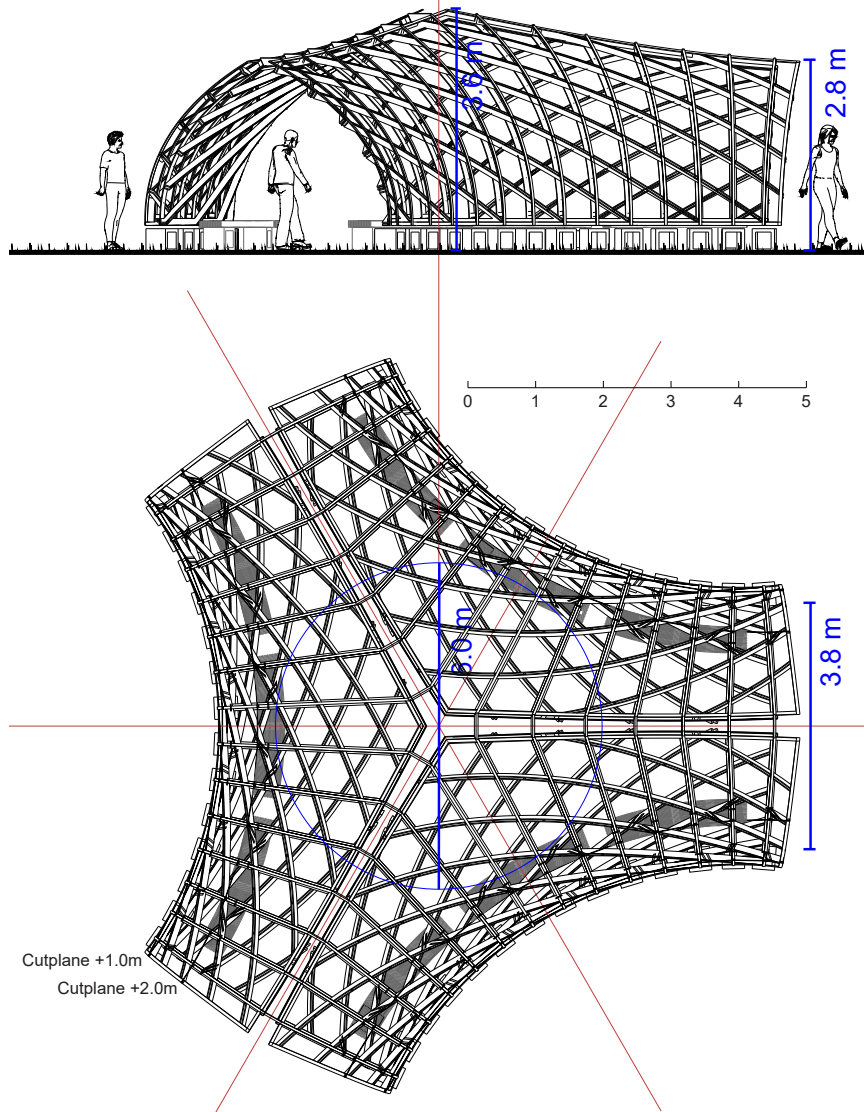

Fig. 2. Plan, Elevation and Visualization of the Asymptotic Geodesic Hybrid Gridshell Design.

2.2.3. Connection details

As illustrated in Fig. 4, there are four typical joints in the structure: 1) Edge to Support (E-S): The gridshell rests on galvanized steel pockets, connecting the timber edge to the concrete supports via 24 mm thick bolts. 2) Asymptotic to Asymptotic (A-A): Asymptotic beams are connected using standardized 24 mm hexagonal studs, which are bolted to the top and bottom beams. 3) Asymptotic to Geodesic (A-G): Geodesic planks are simply connected to the coupling blocks of the asymptotic beam with a single screw. 4) Edge to Edge (E-E): The three shells are

connected along the top edge using parallel steel blades combined with timber couplings.

2.2.4. Complete structure

The timber gridshell features an outer diameter of approximately 10 m. The span at the opening is 3.9 m, encompassing a free interior space with an approximate diameter of 6.0 m and a height of 3.6 m (see Fig. 2). The structure is composed of three shells, covering an area of 60 m². Each shell weighs approximately 300 kg for timber, 30 kg for

Fig. 3. The Asymptotic Geodesic Hybrid Gridshell. Three timber shells are joined to create a negatively curved gridshell. The structure is covered with polycarbonate panels along the geodesic directions. (Photos: Yilinke Tan).
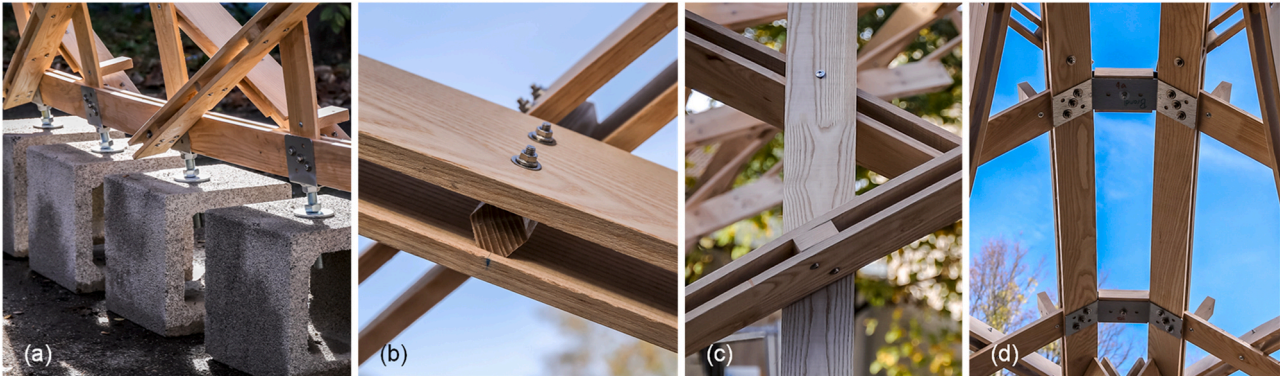

Fig. 4. Connection details. (a): E-S connection, (b): A-A connection, (c): A-G connection, (d): E-E connection. (Photos: Yilinke Tan).

steel screws and plates, and 40 kg for façade panels and aluminum profiles. This amounts to a total weight of 1100 kg for a 100 m² roof area (approximately 11 kg/m²).

2.3. Loading system and measurement

We conducted on-site load tests to study the structural behavior of the gridshell. This experiment focuses on the deformation of the gridshell under two load cases: 1) Local area loading; 2) One-shell asymmetric loading, as shown in Fig. 5. Prior to applying each load case, the initial shape of the prototype is 3D scanned using a Leica RTC360 station, serving as a reference for measuring displacements. Vertical loading is applied by hanging barrels under selected joints and gradually filling them with water. Each barrel is filled with approximately 200 liters of water in 8 steps of 25 liters, resulting in a total load of 9.81 kN on 5 joints for local area loading (Figs. 5a) and 25.51 kN on 13 joints for one-shell asymmetric loading (Fig. 5b). For each load step, the load is sustained for 5 min, allowing the structure to settle under the load. The overall shape of the prototype at each loading stage is then measured by 3D scanning. Simultaneously, the displacements of specific joints are measured using individual trackers (Fig. 6).

Regarding boundary conditions, the lower ends of the geodesic lamellas are considered as supports. The prototype is supported by 42 precast concrete blocks placed directly on the ground. To prevent the supports from sliding on the ground, six belts were installed as horizontal ties between opposite supports, as shown in Fig. 5.

3. Finite element model

An FE model of the constructed Asymptotic Geodesic Hybrid Timber Gridshell prototype was developed using Abaqus/Standard [25], to accurately simulate the physical tests. The model was refined to attribute the softness of joints and supports, which affect the overall deformation behaviour.

3.1. Timber gridshell prototype

The prototype is modelled using beam elements. Based on the digital design model described in Section 2.2, the centrelines of the structural members are used to construct the FE model. The asymptotic and geodesic lamellas are simulated using 2-node Timoshenko beam elements (B31), which have 6 DOFs at each node and consider the shear-deformation effect. A dense mesh (element size less than 0.02 m) is employed in the model to reflect the curvature of each member, ensuring convergence and accuracy. The couplings and connectors are also simulated using B31 elements. The established finite element model of the Timber Gridshell is depicted in Fig. 7. All connections, between families of lamellas and between lamellas and outer frame, are modelled as rigid, except for the geodesic connection, which permits rotation around the local *z*-axis. Slide-plane connectors are utilized to simulate the rotation behaviour of AA joints, based on the simulation result in Section 3.2.

3.2. AA-Joint

The mechanical properties of the joints may significantly impact the overall structural behavior of the gridshell. As discussed in Section 2.2, there are four joint types in the timber gridshell: AA-Joint, AG-Joint, ES-Joint, and EE-Joint. All of these can be modelled as rigid connections, except for the AG joint, which allows rotation in the *xy*-plane. However, upon closer examination, the AA joint exhibits a rotation spring effect around the *y*-axis due to tolerances and softness in the bolted connection of the hexagonal timber stud. Nevertheless, the rotation stiffness around the *z*-axis can be considered rigid because of its hexagonal section.

To evaluate the rotation stiffness of the joint, a refined finite element model is established for half of the AA joint, as shown in Fig. 8. In this refined model, the asymptotic lamellas, the hexagonal stud, and the bolts are all simulated using 8-node linear hexahedral brick elements (C3D8R) with reduced integration and hourglass control. The material
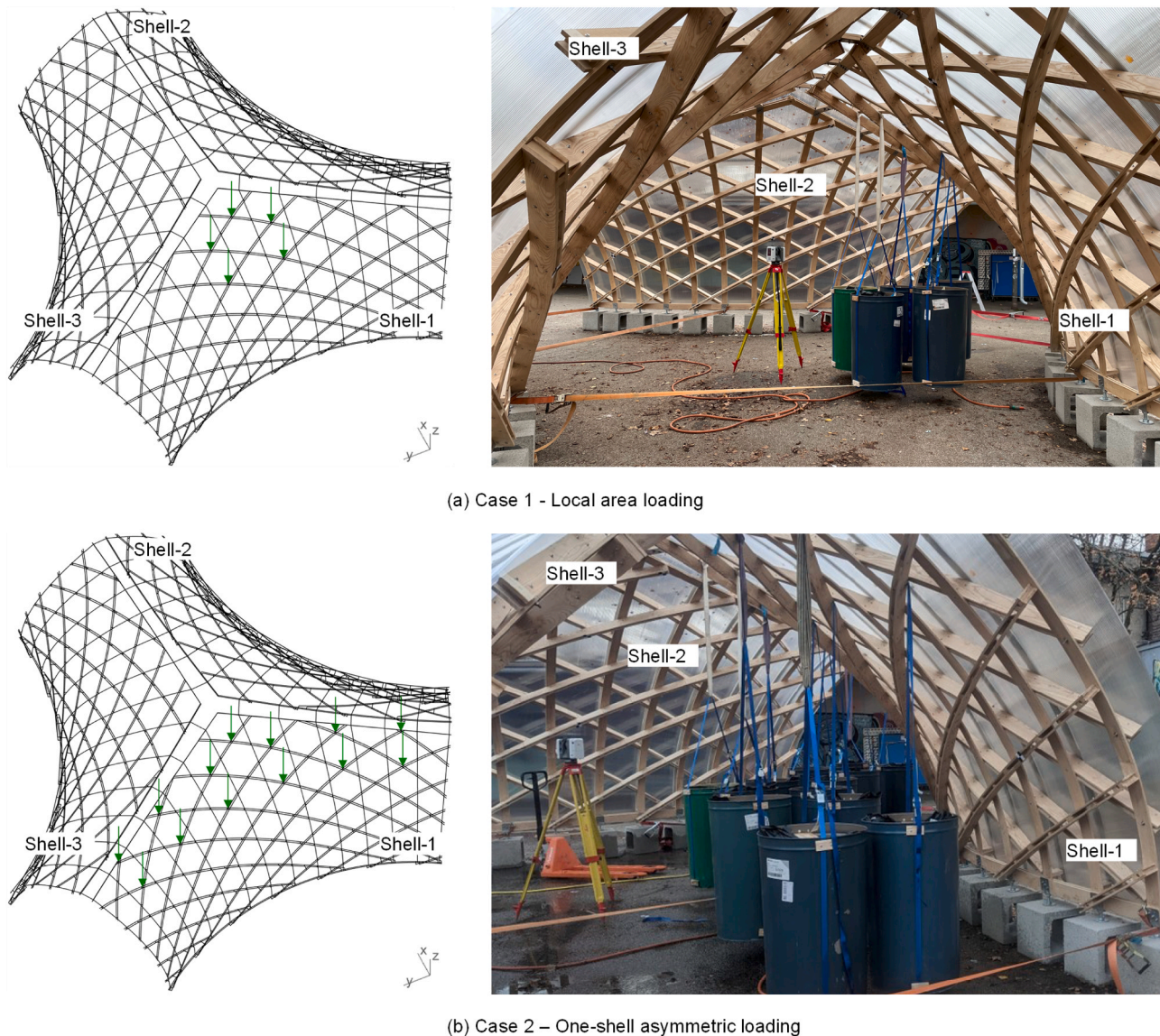
(a) Case 1 - Local area loading

(b) Case 2 – One-shell asymmetric loading

Fig. 5. Test rig showing the loading points for Case 1 – Local area loading; Case 2 – One shell asymmetric loading.

properties used in the FE model are listed in Table 1. A hardwood material model with a strength class D50 is used for the ash timber, obtained from the literature [26] and confirmed by preliminary material testing. In the numerical simulation, wood is assumed to be an orthotropic material, and the elastic modulus of wood under tension and compression is considered equal. The strength in each direction is defined using the Hill yield criterion [27]. The mean values of the strengths are calculated with a variation coefficient of 0.25.

The bolts used in the joints are made of austenitic stainless steel, Grade EN 1.4301, according to the Eurocode [28,29]. The timber material surrounding the bolt holes is much softer than the main region after being drilled [30,31]. It is assumed that this softening effect extends to a region around the hole of no more than 2.5D [30]. Hence, in the finite element model, the Young's modulus of the region around the hole is reduced to 1/23 of the normal region in the grain direction and to 1/6 in the parallel direction [30]. The embedment strengths calculated from the Eurocode [32] are used for the regions around the holes.

The ends of the asymptotic lamellas are fully restrained as boundary conditions. A translational displacement load in the beam direction is applied to a reference point (RP-1), which is coupled to the upper end of the stud. The reaction force F is recorded at the reference point. The bending moment M at the intersection point of the central lines is then

obtained. The moment-rotation relation around the *y*-axis of the AA-Joint is presented in Fig. 9. The rotational behaviour progresses through several stages [33]. Initially, the stiffness is caused by the friction between the rod and the lamellas. When the rod starts to slide (A), the rotation stiffness drops significantly until the bolts begin touching the holes (B). The rotation stiffness gradually increases until all the screws, the rod, and the lamellas fully touch each other (C). Then the rotation stiffness grows more rapidly until the timber rod breaks (D). A simplified moment-rotation relation is defined based on the simulations and is used in the finite element model of the overall prototype.

3.3. Supports

To prevent the supports from sliding on the ground, six belts were employed as horizontal ties between opposing supports. These belts elongate as the supports slide, thereby increasing tension/horizontal reaction during external loading. The interaction effects of vertical reaction force, horizontal reaction force (friction), and tension in the belts form a highly coupled and complex relationship. As illustrated in Fig. 7, the FE model incorporates a series of zero-length Slide-Plane connectors between the supports and the ground to simulate vertical constraint and horizontal friction behaviours. This approach ensures that the vertical
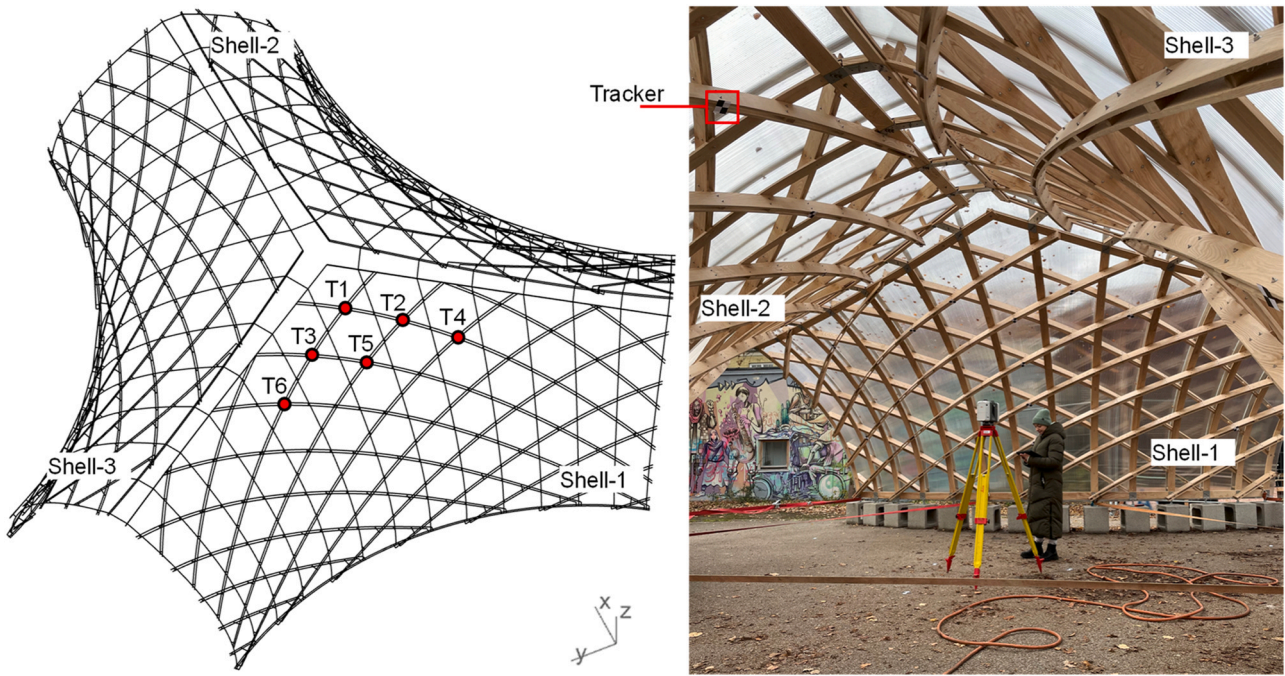
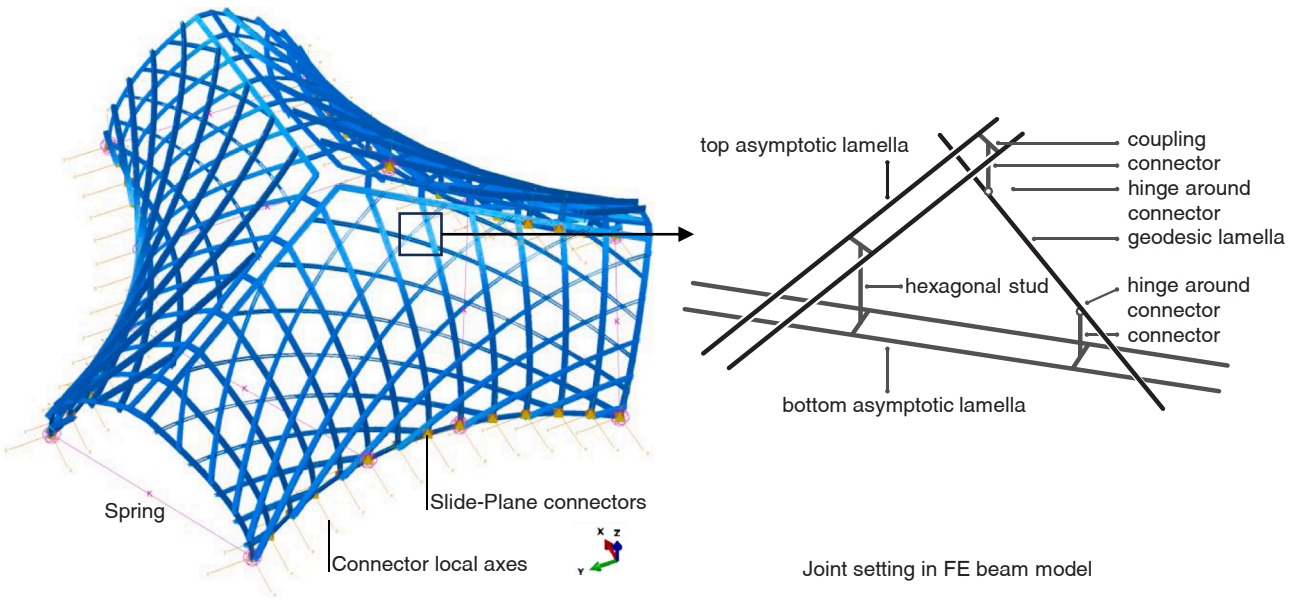**Fig. 6.** Set-up for monitoring points using individual trackers.

Fig. 7. Finite element model for the timber gridshell.

translational freedom (in the local *x*-axis) of all supports is constrained to bear vertical loads (in the global *z*-axis). The maximum friction is consistently determined by the vertical reaction force and the friction coefficient, which is set as 0.62. To replicate the restraining function of the belts between the supports, six spring elements are employed in the finite element model. The shorter three springs exhibit an axial stiffness of 50000 N/m, while the longer three springs have an axial stiffness of 41212 N/m.

3.4. Initial stress and residual stress

An implicit nonlinear solver is chosen to calculate the structural response considering the large deformations of the structure. The simulation considers gravity and external live loads, which are applied

in two steps.

The erection process of the gridshell additionally causes initial stresses by elastic bending and twisting of the timber lamellas. The influence of these initial stresses on load-bearing behavior and stiffness has been investigated for steel in a previous publication [19]. In this study, the Saint-Venant torsional shear stress and the initial normal stress due to Helix-Torsion [34] are calculated based on the geodesic torsion using the same analytical method described in [19]. Moreover, the initial bending stress is calculated analytically considering the different geometric curvatures of asymptotic and geodesic lamellas. Based on the beam theory of Euler-Bernoulli [20], the initial bending stress caused in the erection process can be computed using Eq. (1&2). The lamellas are only bent around the weak axis, to achieve the bending curvature k: the geodesic curvature k_g for asymptotic members and the
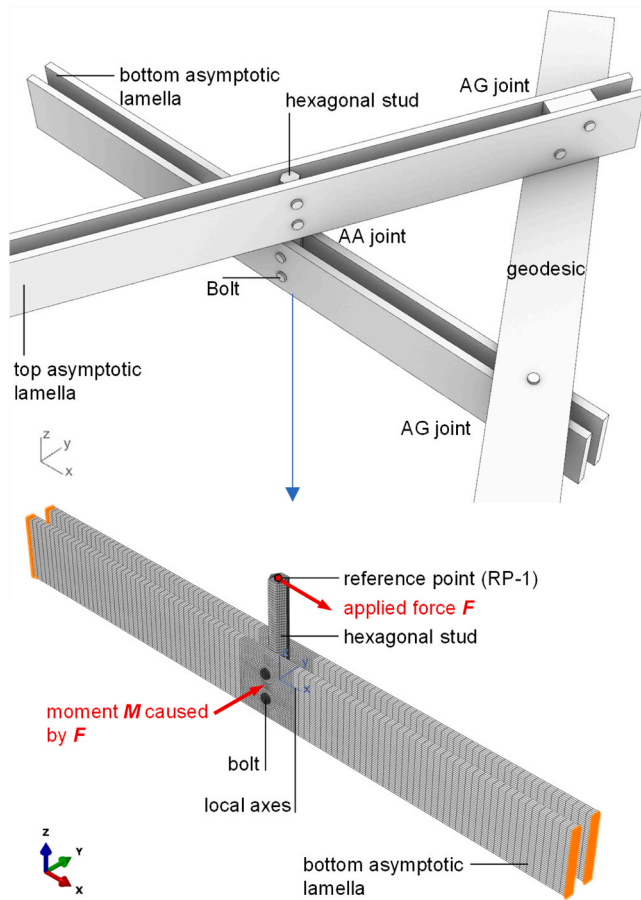
Fig. 8. Simplification and Finite Element modelling for the AA-Joint.

normal curvature k_n for geodesic members. For each lamella, the maximum bending stress σ_{max} in any cross-section is related to Young's modulus E, lamella thickness t and its bending curvature k at this position:

$$k = \frac{1}{r} = \frac{M}{EI} = \frac{W\sigma_{max}}{EI} = \frac{2\sigma_{max}}{Et} \quad (1)$$

$$\sigma_{max} = \frac{E \bullet t \bullet k}{2} \quad (2)$$

where M is the local bending moment, $W = t^2 h/6$ is the section modulus, $I = t^3 h/12$ is the moment of inertia, t and h are the lamella thickness and height, r is the bending radius.

However, timber is a natural material with special properties in different conditions. Keeping sprinkling water on the timber elements ensures its high moisture will maintain its bendability throughout construction [6,35]. During construction, water was used to treat the critical areas of the structure, and the timber structure was exposed to rain before the cladding installation, as well as changing humidity and temperature in an outdoor environment. No failure due to excessive bending was recorded in the timber structure during construction or load testing. After construction, the initial stress generally decays over time due to the stress relaxation effect of timber, hence leading to

residual stress in the members [36]. According to the experiments on spruce lamellas by Aondio [37], the following formula is recommended to determine the stress relaxation effect:

$$\sigma_{\infty} = \sigma_0 \bullet \frac{1}{1 + k_{def}} \quad (3)$$

where σ_0 is the initial stress from the construction process, σ_{∞} is the residual stress due to the stress relaxation effect, k_{def} is the deformation coefficient based on service class from DIN 1052:2008–12. For the ash timber vault in this study, $k_{def} = 2.0$ (service class 3). The residual stress remains approx. 33% of the initial stress in the members, as illustrated in Fig. 10. The analysis results indicate that bending stress is the predominant factor contributing to the initial stress levels, while the stress induced by torsion plays a comparatively minor role. The result is then used to evaluate the load-bearing capacity in the following sections.

4. Test results and validation of simulation method

To validate our digital simulation, we compare the deformation behaviour along two physical tests. We compare the displacement graphs of physical data and the corresponding simulation.

4.1. Local area loading

In the first load case, the vertical loads are applied to a small local region of one shell, reflecting its structural performance to take local loads.

Fig. 11 presents the vertical deformation and the stress distribution (without residual stress) of the prototype under various loading stages, as captured by both 3D scanning and digital simulation. It is observed that the deformation in the loaded zone aligns with the direction of the external load, while the unloaded zone experiences a slight upward deformation. To calculate deformation from the 3D scanning results, the M2C3 algorithm within CloudCompare [38] is employed, which compares point clouds between different loading stages. However, a clear point relationship between the measured stages in the laser scan data is lacking. The M2C3 algorithm utilizes a "normal orientation" in the $+z$-axis direction to define the search direction for the neighbourhood relation between point clouds. This method can introduce some error when components are relatively vertical and align with the "normal orientation". For example, the geodesic planks in the front part of the perspective are relatively vertical, resulting in a reddish hue that
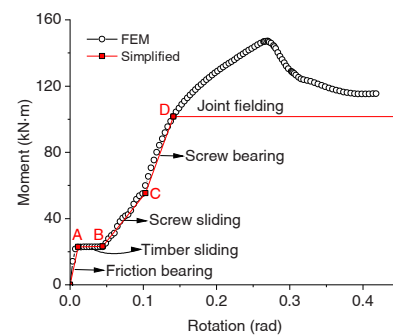

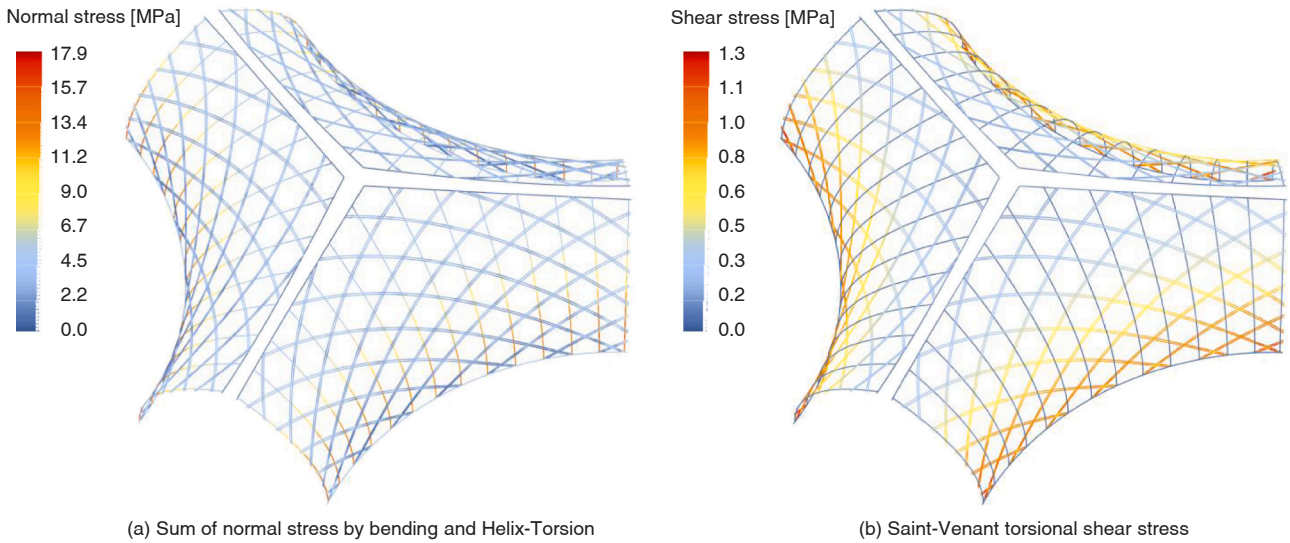**Fig. 9.** Moment-rotation relation around the y-axis of the AA-Joint.

Table 1
Material properties of lamella and bolts used in the FE models [26].

Component	Elastic modulus (MPa)			Poisson's ratio			Shear modulus (MPa)			Strength (MPa)				Density (kg/m³)
	E_L	E_T	E_R	μ_{LR}	μ_{LT}	μ_{RT}	G_{LR}	G_{LT}	G_{RT}	$f_{c,L}$	$f_{c,T}$	$f_{c,R}$	$f_{s,R}$	ρ
Lamella	14000	700	1400	0.45	0.45	0.3	880	1050	252	85.1	10.6	10.6	7.7	740
Bolt	$E = 2.06 \times 10^5$			$\mu = 0.3$			$G = 0.79 \times 10^5$			$f_m = 223.4$				7850

(a) Sum of normal stress by bending and Helix-Torsion

(b) Saint-Venant torsional shear stress

Fig. 10. Residual stress equivalent to 33% of the initial stress due to the erection process.
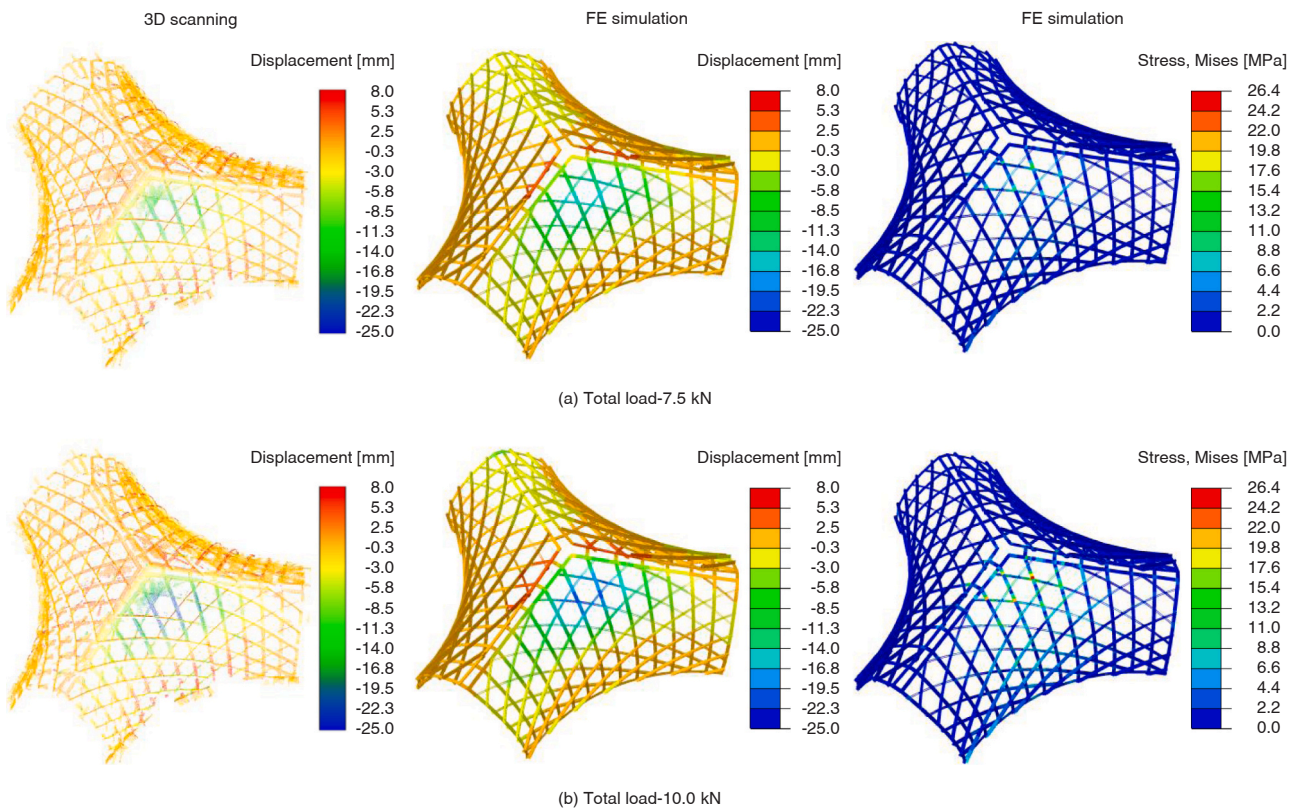

(a) Total load-7.5 kN

(b) Total load-10.0 kN

Fig. 11. Vertical displacement and stress distribution of the prototype at different loading stages for local area load case (left-scanning results, right-FEM results).

contrasts with the green or blue colour of the asymptotic planks. Furthermore, in the middle span, the asymptotic planks are relatively vertical, leading to a larger error in the results when compared to the geodesic planks. Fig. 12 provides a more precise comparison of the load-displacement curves for joints T1, T2, T4, and T5 (refer to Fig. 6) between the physical experiment and the digital simulation. The deformation results from the physical experiment are measured using individual trackers. As the load increases to 2.0 kN for each joint, the maximum displacement reaches 25 mm. Notably, there is no evidence of buckling or breakage observed throughout the loading process. From the FE simulation, the maximum stress of 26.4 MPa is found in the geodesic

lamellas around the loading position at the last loading stage. If we consider the residual stress of around 4.0 MPa shown in Fig. 10 at that position, the total stress would be 30.4 MPa, still within the characteristic strength of the adopted ash timber (50.0 MPa).

The deformation simulation results are highly consistent with the experimental results from the individual trackers, validating the finite element modelling method.

4.2. One-shell asymmetric loading

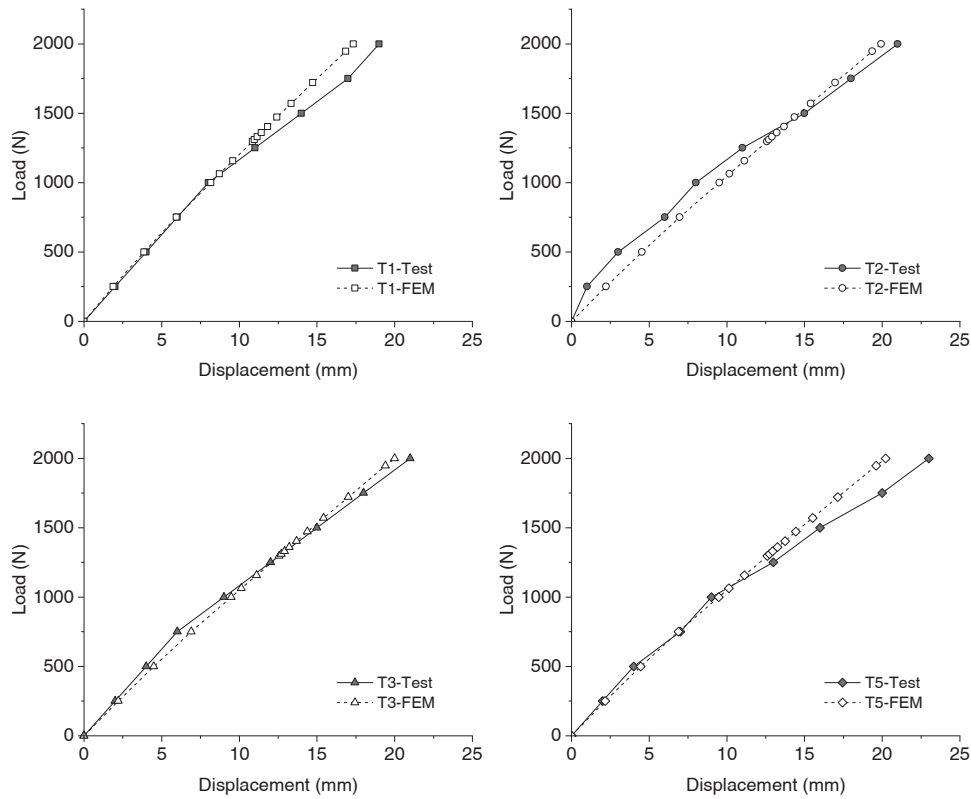In the second case, the load is applied to the whole region of one

Fig. 12. Load-displacement behaviours of different joints under local area loading.

shell, which reflects the structural behaviour under asymmetric load.

The structure was scanned at each loading stage, and the vertical displacement and stress distribution (without residual stress) is shown in

Fig. 13 for two different loads. The point cloud illustrates the vertical deflections, which were confirmed by individual trackers at a maximum of − 35 mm. Nonetheless, the issue of "normal orientation" when

(a) Total load-19.5 kN

(b) Total load-26.0 kN
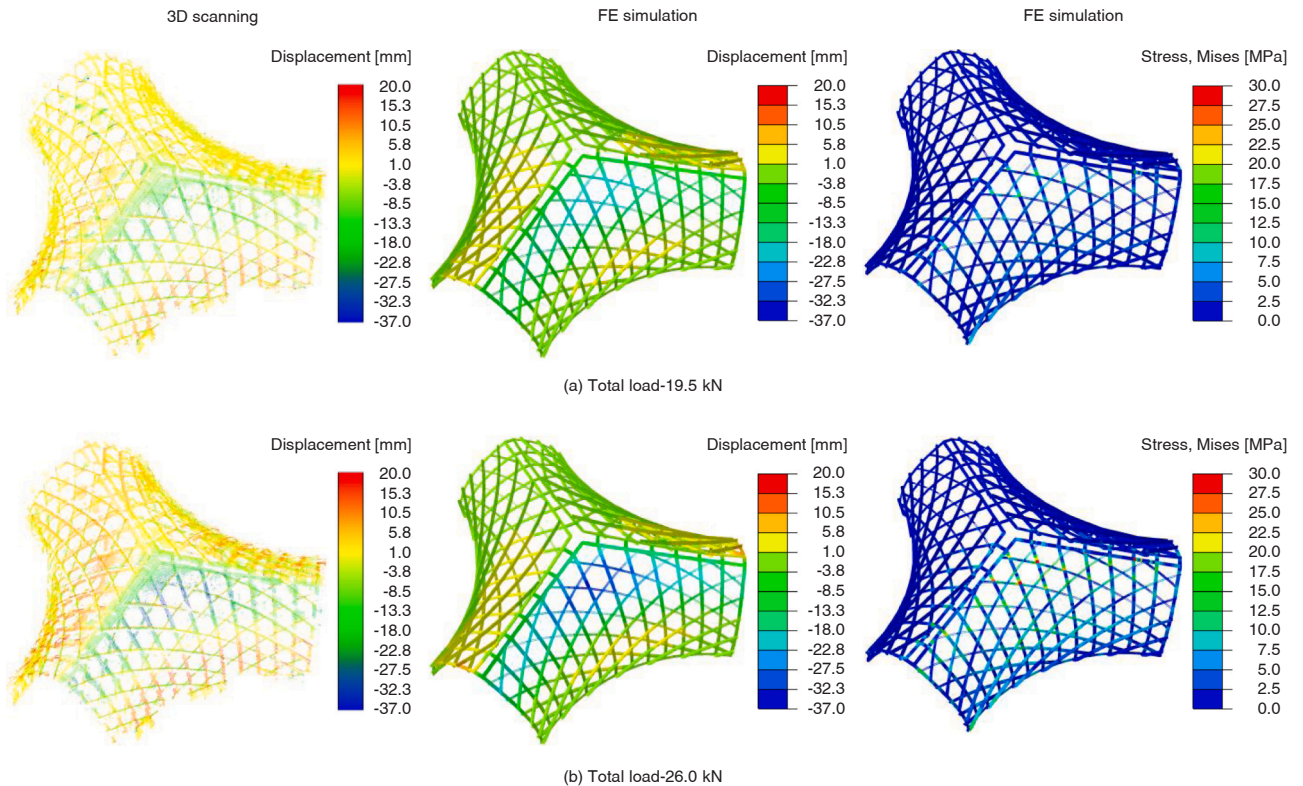
Fig. 13. Vertical displacement and stress distribution of the prototype at different loading stages for asymmetric load case (left-scanning results, right-FEM results).

comparing point clouds, as discussed in the previous section, continues to contribute to some inaccuracies in the 3D scanning displacement results. The load-displacement curves of trackers T1–6 (see Fig. 6) are compared with the simulation results in Fig. 14. The structural behaviour demonstrates a degree of nonlinearity during loading, which primarily arises from the sliding-friction conditions of the supports. The test results obtained from individual trackers provide strong validation for the FE simulations. In this case, the maximum stress of 30.0 MPa is caused by the external load at the same location where the maximum stress was found in the case of local area loading. Considering the residual stress of around 4.0 MPa at that position, the total stress would be 34.0 MPa, which is below the characteristic strength of ash wood.

At the later loading stage, creaking noise could be heard from the structure when filling water into the barrels, which was caused by the friction at the joints. During this test, no failure, cracking, or sudden movement of the structure was recorded.

5. Parametric analysis of AAG hybrid gridshells

Based on the validated FE model, a parametric analysis is conducted to investigate the influence of the polar array layout, the joint stiffness, and the support condition on the structural performance of the timber gridshell. For this purpose, an idealised FE model with polar arrayed shells was created, which is used as a basic design for the parametric research. The supports are fixed in three directions to simulate the hinged supports of an ideal construction design. Unless stated otherwise, the joints within the model are assumed to be completely rigid. The structure is investigated under a homogeneous distributed load of 1.0 kN/m^2 on the horizontal projection plane, applied as point forces at the AA joints for the full span. The displacement in the global z-direction of the monitoring point (T5) is adopted to generate load-displacement curves.

5.1. Structural behaviour under full-span distributed load

The typical behaviour of semi-spherical shell under full span load
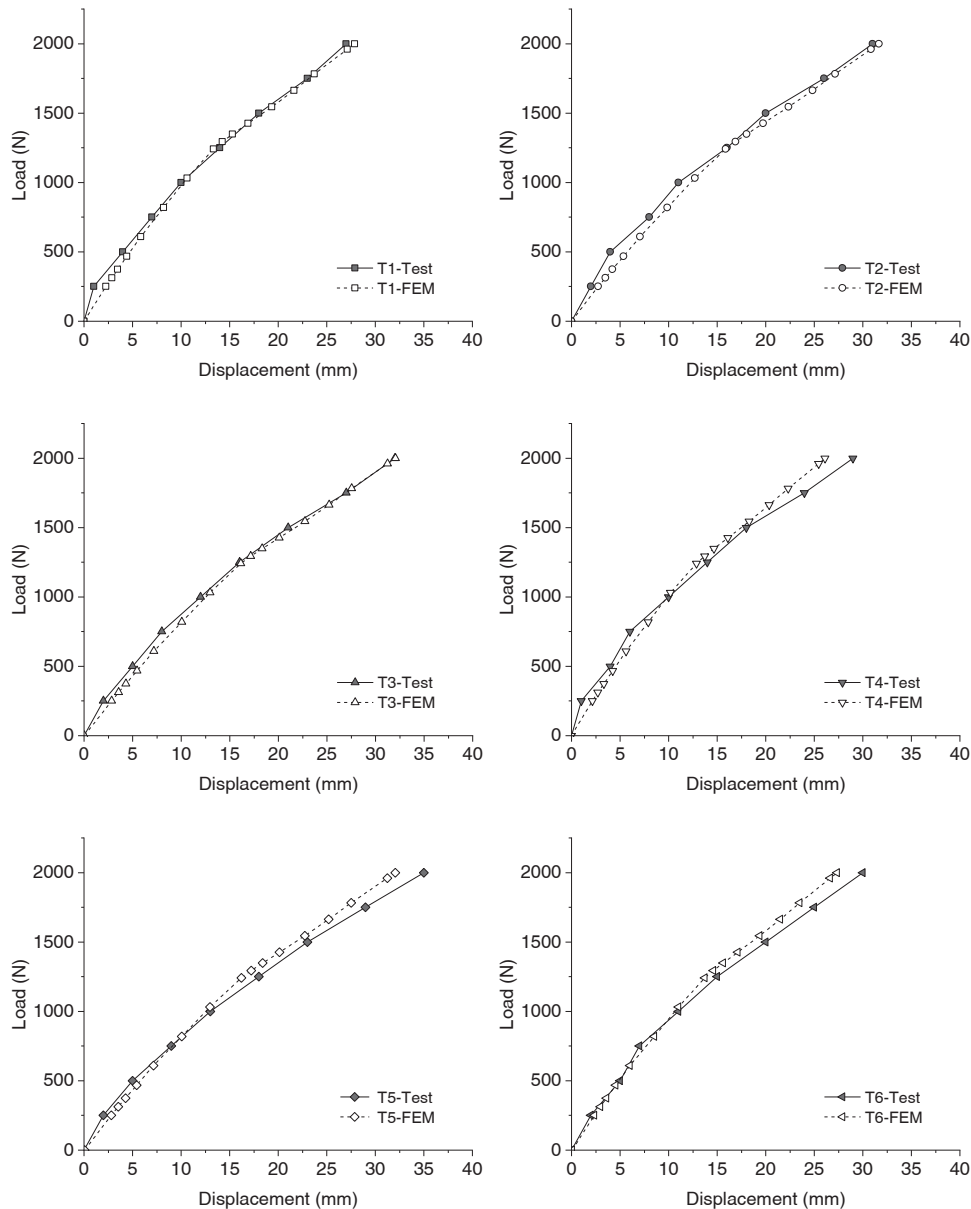

Fig. 14. Load-displacement behaviours of different joints under asymmetric loading.

results in compression rings above 52° and tension rings below [39]. The prototype investigated in this paper displays the inverse behaviour (Fig. 15) under self-weight and a full span uniform load of 1.0 kN/m², due to its negative Gaussian curvature. The top parts of the three shells undergo inwards deformation, resulting in a horizontal elongation of the negatively curved grid. Consequently, tension forces are generated in the asymptotic elements, and compression forces emerge in the geodesic lamellas. Conversely, the bottom parts of the shells undergo outward deformation, resulting in the contraction of the asymptotic members, causing compression. The diagonal asymptotic grid would naturally undergo a scissor movement, which is prevented by the vertical geodesic planks. This effect leads to a decrease of the compression in the geodesic planks. Fig. 16 presents the corresponding stress distribution in the members caused by the external load. To estimate the influence of the residual stress (Fig. 10), three positions are checked to determine the total stress level. Position 1 exhibits high stress due to external load and low residual stress. Position 2 shows approximately equal residual stress and load-induced stress. Position 3 features a much higher residual stress and a smaller load-induced stress. The results are listed in Table 2. Through the comparison, Position 3 has the maximum stress of 21.3 MPa, which is below the characteristic strength of ash wood.

The combination of geodesic and asymptotic lamellas creates an exceptionally efficient tri-hex gridshell. The asymptotic lamellas offer stiffness in the out-of-plane direction, while the planar geodesic lamellas provide stiffness in the in-plane direction and minimize the buckling length. This configuration enables the structural system to effectively distribute load through a membrane-like force flow.

5.2. Polar array layout

In the constructed prototype, one of the shell elements was pre-fabricated with top and bottom lamellas swapped. This creates a symmetric appearance at the two entrances (see Fig. 3), where the bottom layer of lamellas is nicely mirrored. However, this architectural decision has an effect on the load-bearing behaviour of the three shells, as they do not strictly follow a polar array layout.

To investigate the influence of this inconsistency, Fig. 17 compares the deformation modes of the timber gridshells of the constructed prototype and the ideal model, following a polar array, at a full-span uniform load 4.0 kN/m². As can be seen, the deformation magnitudes are not the same within the three shells of the constructed prototype. In contrast, the three shells in the ideal model deform simultaneously with the same magnitude. The maximum deformation of the constructed model is about 34 mm, which is significantly larger than 28 mm
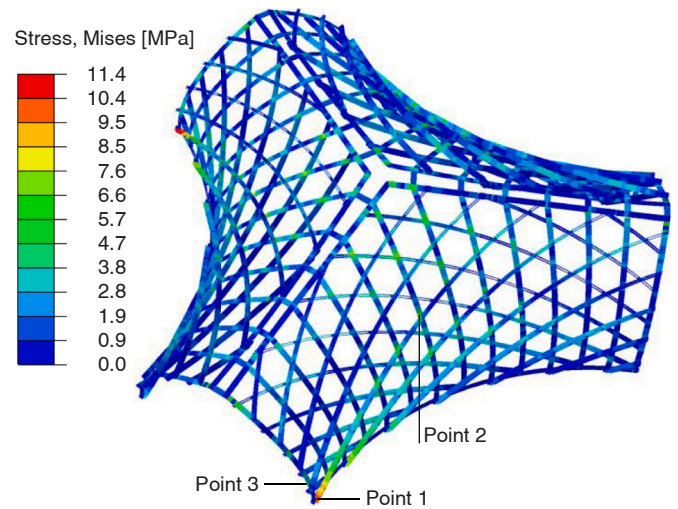

Fig. 16. Stress distribution of the timber gridshell under self-weight and a full-span homogenous load of 1.0 kN/m².

Table 2
Normal stress in lamellas (MPa).

Position	Residual stress	Load- induced stress	Sum
Point 1	5.8	11.4	17.2
Point 2	7.3	7.2	14.5
Point 3	17.9	3.4	21.3

observed in the ideal model. Fig. 18 presents the load-displacement curves obtained from the simulation for Points 4, 5 and 6 under a full-span uniform distributed load. For the ideal model, it has been predicted that at Position 1 (marked in Fig. 16), the cumulative stress reaches the characteristic strength of 50 MPa when subjected to a load of 4.5 kN/m², and attains the mean strength of 85.1 MPa under a load of 7.0 kN/m², which is defined as the ultimate state in this paper. The swapping of the layer arrangement within the third shell evidently brings a negative influence on the structural behaviour of the whole system.

5.3. Joint rotation stiffness

As discussed in Section 3.2, the AA-joint functions as semi-rigid
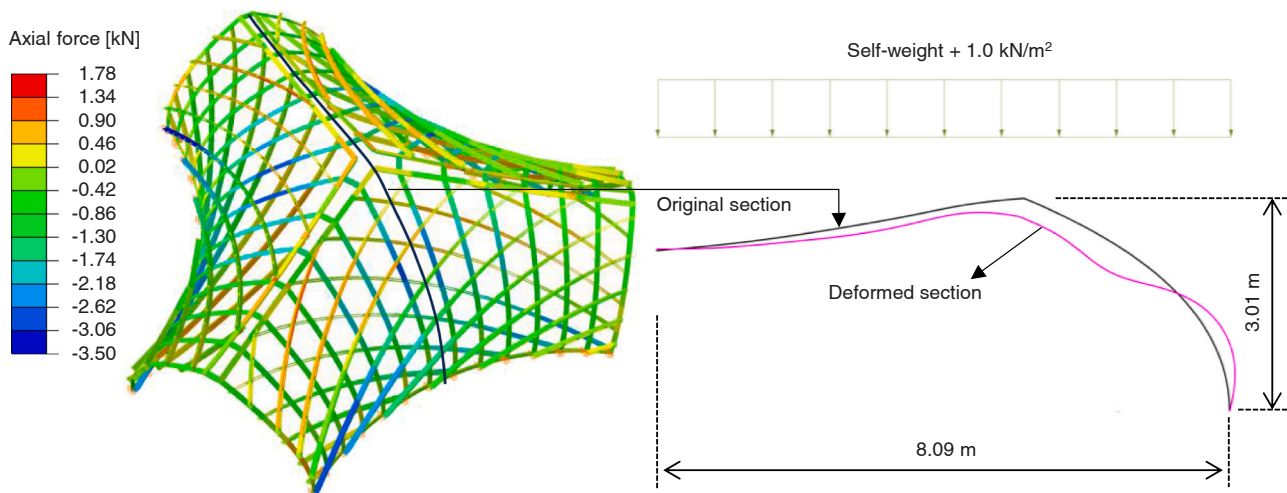

Fig. 15. Axial force (left) and section deformation mode (right) of the timber gridshell under self-weight and a full-span homogenous load of 1.0 kN/m². At right, the deformation is scaled by 80.
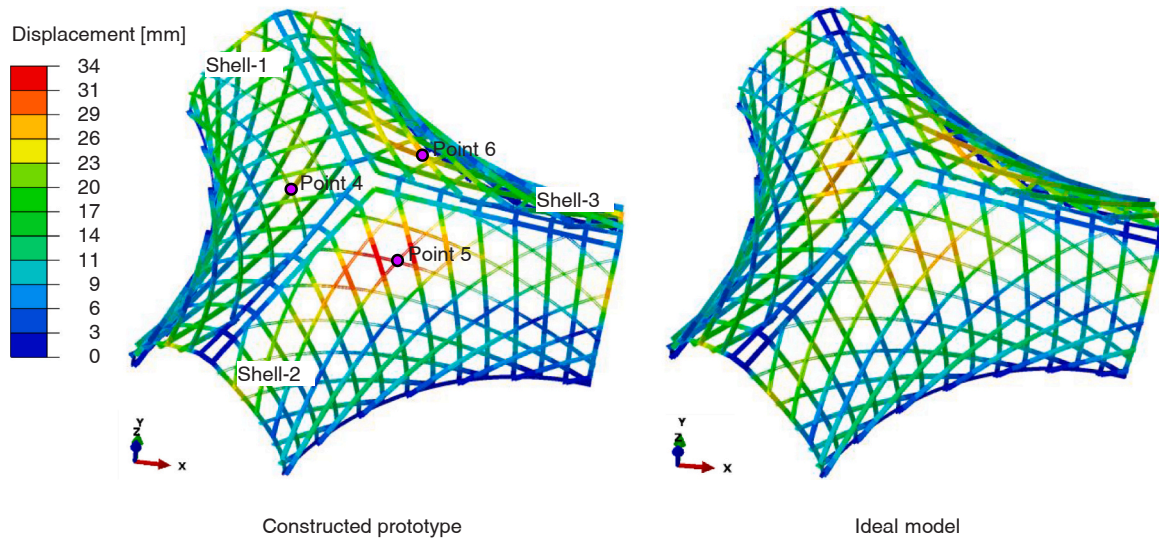
Fig. 17. Deformation distribution of the timber gridshells at a full-span load of 4.0 kN/m².
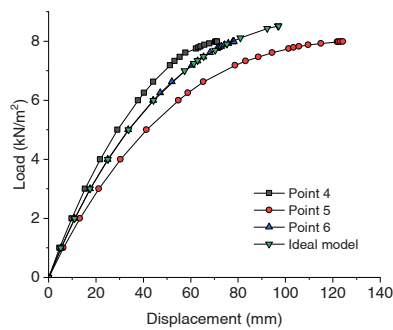

Fig. 18. Influence of geometric symmetry on load-displacement behaviours under full span loading.

connection in the *xz* plane. To investigate the impact of connection rigidity, the load-displacement curves of the structures with different rotation stiffness joints under full-span load are presented in Fig. 19. The rotation stiffness of the semi-rigid joints is obtained from FE simulations of the joints in Section 3.2. The model with rigid joints behaves with similar stiffness to the one with hinge joints around local *y*-axis at early loading stage. However, the fully rigid joints can enhance the structural behaviour at the later loading stage.

The rods within the AA-joint cannot directly transfer forces from the top asymptotic members to the bottom ones along their axial directions (*x*-axis), and vice versa. Therefore, the long continuous asymptotic members primarily distribute their axial forces to the geodesic members
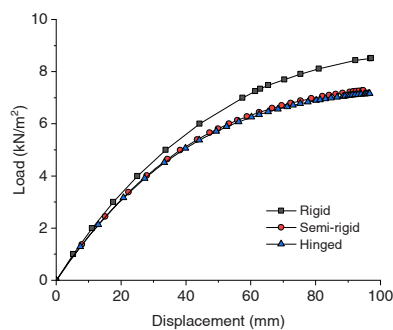
through AG-joints. The tri-hex grid of hybrid geodesic and asymptotic lamellas ensures a stable gridshell system, which mainly generates axial forces in the elements.

5.4. Support condition

In the constructed model, the supports are not perfectly fixed on the ground, and they can slide slightly during the loading stage even though six belts are used to constrain their movement. To quantify the influence of the support sliding, the symmetric model is analysed with the same support condition as the constructed prototype under full-span loading. Fig. 20 compares the load-displacement curves of the timber gridshells with fixed supports and sliding supports. Due to the sliding behaviour of the supports, the vertical displacement exhibits a stronger nonlinearity with increasing load. The movement of the supports significantly weakens the overall stiffness of the structure and reduces its load-bearing capacity from 7.0 kN/m² to 6.2 kN/m², illustrating the importance of horizontal support constraints.

6. Achievable scale for future architectural applications

This section investigates the fundamental factors influencing the scale that the timber gridshell can achieve from a practical design perspective in terms of both stiffness and strength. We maintain the shape of the structure and synchronize the enlargement of all dimensions within the structure, including the span, grid size, cross-section size, etc. In this study, the span of the gridshell is measured at the three openings, which are 3.9 m at the current scale (see Fig. 2).

Fig. 19. Influence of joint rotation stiffness on load-displacement behaviours under full-span loading.
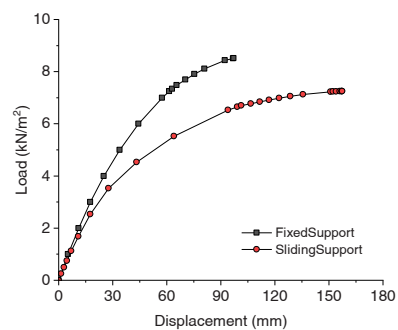

Fig. 20. Influence of support condition on load-displacement behaviours under full-span loading.

Throughout this study, ash is consistently utilized as the construction material.

6.1. Initial bending stress

According to Eq. (1), for all the asymptotic and geodesic planks, the relation between the maximum bending stress σ_{max} in any cross-section, lamella thickness t and its bending curvature radius r at this position can be written as:

$$\sigma_{max} = \frac{E \bullet t}{2 \bullet r} \tag{3}$$

After enlarging the dimensions, the curvature radii r of the structural members is also scaled synchronously with the same ratio. From Eq. (3), the distribution of the initial bending stresses in the members remains constant after scaling up the structure [40], which means that the scaled thickness of the lamellas still meets the requirements to avoid any breaking during construction but cannot be increased additionally. The same principle is found when considering the Saint-Venant torsional shear stress and the initial normal stress due to Helix-Torsion.

6.2. External load

In the investigation, we consider two design criteria: the ultimate limit state for strength; the serviceability limit state for stiffness. The structural response of the timber gridshell at different scales is analysed by performing three load cases, Case-P: prestress (residual stress), Case-G: structure self-weight and Case-S: uniformly distributed snow load (a load uniformly distributed throughout its projection plane 1.15 kN/m^2).

6.2.1. Strength

Based on the FE simulations, Fig. 21 plots the maximum stress of three critical points of the structure for the two load cases and their combinations with the increasing span. The monitoring points are referred to Points 1, 2 and 3 shown in Fig. 17. In this calculation, we consider the partial safety factors for the load cases and fundamental combination 1.0 P + 1.35 G+ 1.5 S [41]. The stress is positively linear with respect to the span for the self-weight, whereas it remains constant for the snow load.

This principle can also be obtained using dimensional analysis [40]. Since the self-weight load is proportional to the cubic of the scale, and the snow load is proportional to the quadratic of the scale, there is a positive linear relationship between the stress distribution and the span under self-weight; while under uniform snow load, the stress distribution remains constant. In any section of the timber lamella, with the local bending moments M_y, M_z and the axial force N, the axial stress can be expressed as:

$$\sigma_{max} = \sigma_1 + \sigma_2 + \sigma_3 = \frac{M_y h}{2I_y} + \frac{M_z t}{2I_z} + \frac{N}{A} \tag{5}$$

where $A=ht$, $I_y=th^3/12$, and $I_z=t^3h/12$.

For self-weight load, with the density ρ, the gravitational acceleration g, the volume of the material V and coefficients a_1, a_2, a_3, a, the axial stress can be written as:
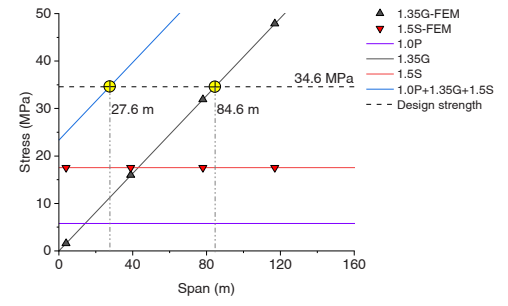
$$\sigma_{max} = \frac{(a_1\rho g Vl)h}{2I_y} + \frac{(a_2\rho g Vl)t}{2I_z} + \frac{a_3\rho g V}{ht} = a\rho g l \tag{6}$$

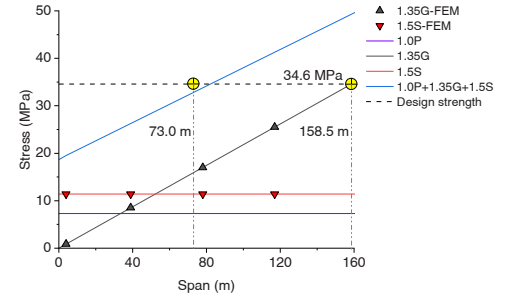where $M_y=a_1\rho g Vl$, $M_z=a_2\rho g Vl$, and $N=a_3\rho g V$.

It is observed that the stress distribution is linear with the span under self-weight.

For homogenous snow load, with the fixed surface load $q=$ 1.15 kN/m^2 and coefficients b_1, b_2, b_3, b, the axial stress can be written as:
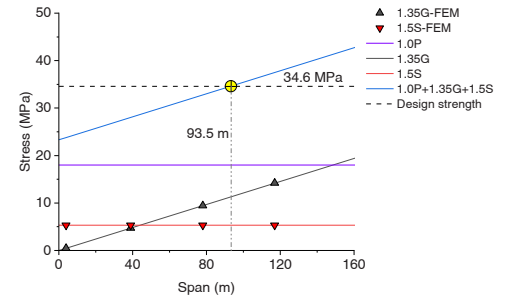
$$\sigma_{max} = \frac{(b_1 q l^3)h}{2I_y} + \frac{(b_2 q l^3)t}{2I_z} + \frac{b_3 q l^2}{ht} = bq \tag{7}$$

(a) Position 1

(b) Position 2

(c) Position 3

Fig. 21. The stress σ at Positions 1, 2 and 3 in relation to span l.

where $M_y=b_1 q l^3$, $M_z=b_2 q l^3$, and $N=b_3 q l^2$.

It is found that the stress distribution remains constant with increasing the span under snow load.

According to Eurocode [32], the design strength of the ash material is taken as

$$f_d = k_{mod}\frac{f_k}{\gamma_M} = 0.9 * \frac{50}{1.3} = 34.6\text{MPa} \tag{4}$$

where f_k is the characteristic value of a strength property, γ_M is the partial factor for a material property, k_{mod} is a modification factor considering the effect of the duration of load and moisture content.

Under the load combination 1.0 P + 1.35 G + 1.5 S, the maximum span of the structure can reach 27.6 m, provided that the stresses are kept below the allowable limits. This corresponds to a scale factor of 7 compared to the current prototype and would result in an inner dome with a diameter of 42 m.

6.2.2. Stiffness

Based on the FE simulations, Fig. 22 shows the ratio of the maximum displacement to span (d/l) of the structure for the two load cases and their combinations with the increasing span. The monitoring point is referred to Points 4, 5 or 6 shown in Fig. 17. In this regard, the characteristic combination of self-weight and snow load (1.0 G+1.0 S) is considered in the structural analysis. The ratio d/l is positively linear with respect to the span l for the self-weight, whereas it remains constant
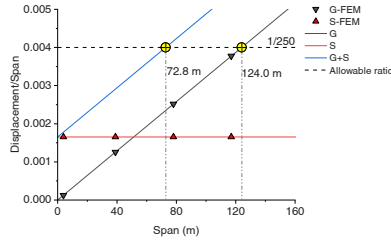
Fig. 22. The ratio d/l in relation to l (with span l, displacement d).

for the snow load.

This law can also be obtained from the dimensional analysis. Based on the research in Reference [21], under the action of the total load F, the maximum deformation d can be expressed using an analytical solution:

$$d = d_1 + d_2 + d_3 + d_4 + d_5 = k_1\frac{Fl^3}{El_y} + k_2\frac{Fl^3}{El_z} + k_3\frac{Fl^3}{GI_t} + k_4\frac{Fl}{GA} + k_5\frac{Fl}{EA} \quad (8)$$

where $A=ht$, and $I_t=0.309t^3h/3$ for this perticular section.

In this formula, the displacement d is divided into four parts: d_1, caused by bending moment around strong axis; d_2, caused by bending moment around weak axis; d_3, coming from torsion; d_4, shear deformation; and d_5, coming from axial force. The coefficients k_1, k_2, k_3, k_4 and k_5 are related to the structure geometry, the boundary condition, and the load case.

For self-weight load, with coefficients m_1, m_2, m_3, m_4, m, the ratio d/l can be written as:

$$\frac{d}{l} = m_1\frac{(\rho gV)l^2}{EI_y} + m_2\frac{(\rho gV)l^2}{EI_z} + m_3\frac{(\rho gV)l^2}{GI_t} + m_4\frac{(\rho gV)}{GA} + m_5\frac{(\rho gV)}{EA} = m\frac{\rho g}{E}l \quad (9)$$

It is observed that the ratio d/l is linear with the span under self-weight.

For homogenous snow load, with coefficients n_1, n_2, n_3, n_4, n, the ratio d/l can be written as:

$$\frac{d}{l} = n_1\frac{(ql^2)l^2}{EI_y} + n_2\frac{(ql^2)l^2}{EI_z} + n_3\frac{(ql^2)l^2}{GI_t} + n_4\frac{(ql^2)}{GA} + n_5\frac{(ql^2)}{EA} = n\frac{q}{E} \quad (10)$$

It is found that the ratio d/l remains constant with increasing the span under snow load.

Under the load combination (1.0 G+1.0 S), the maximum span of the structure can reach 72.8 m under the condition that the radio d/l is smaller than the allowable limit (1/250).

6.2.3. Buckling behaviour

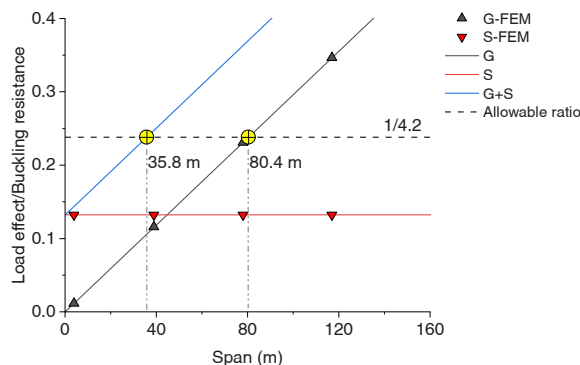Fig. 23 illustrates the ratio of the load effect S to the buckling resistance R of the structure for the two load cases and their combinations as the span increases. As in Section 6.2.2, the characteristic combination of self-weight and snow load (1.0 G+1.0 S) is considered. Based on Eigenvalue Buckling Analyses, it is found that the first-order buckling mode is about compression buckling in geodesic lamellas at the middle area of each shell for both Case-G and Case-S.

From FE simulations, the ratio exhibits a positive linear relationship with respect to the span l for self-weight, while it remains constant for snow load. This law can also be obtained from the dimensional analysis. For any compressive element in the gridshell, the critical buckling resistance R is calculated by the Euler's formula:

$$R = P_{Cr} = \frac{\pi^2 EI_z}{(KL)^2} \quad (11)$$

where P_{Cr} is Euler's critical load, L is the unsupported length of the element, K is effective length factor.

For self-weight load, with coefficients α_1, α, the ratio S/R can be written as:

$$\frac{S}{R} = \alpha_1\rho gV \left/ \left(\frac{\pi^2 EI_z}{(KL)^2}\right)\right. = \alpha\frac{\rho g}{E}l \quad (12)$$

It is observed that the ratio S/R is linear with the span under self-weight.

For homogenous snow load, with coefficients β_1, β, the ratio S/R can be written as:

$$\frac{S}{R} = \beta_1 ql^2 \left/ \left(\frac{\pi^2 EI_z}{(KL)^2}\right)\right. = \beta\frac{q}{E} \quad (13)$$

It is found that the ratio S/R remains constant with increasing the span under snow load.

Under the load combination (1.0 G+1.0 S), the structure's maximum span can reach 35.8 m, provided that the ratio S/R remains below the allowable limit (1/4.2). However, no codes specify this allowable limit for this linear elastic buckling analysis. Consequently, the value of 1/4.2 for nonlinear elastic analysis is derived from a Chinese technical specification [42]. This section primarily examines the qualitative impact of buckling problems on span.

As the structure's span increases, the stresses, displacements, and buckling induced by self-weight account for a larger proportion, ultimately limiting the maximum scale. While the lamella section's thickness and height are constrained by the curves' curvature, the structural stiffness and ultimate load-carrying capacity could be enhanced by increasing the mesh density [21] or the distance between double lamellas [22].

7. Conclusion

This paper presented the experimental and numerical investigations on the structural behaviour of an asymptotic geodesic hybrid gridshell

Fig. 23. The ratio of load effect S to buckling resistance R in relation to span l.
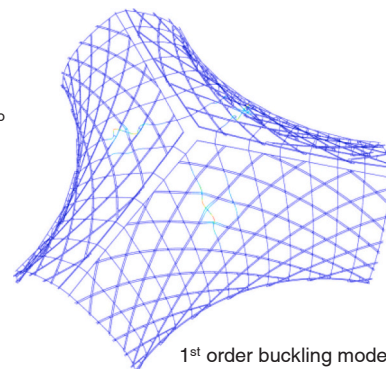
system. The structures enable convenient construction of doubly curved gridshell only from standardized timber plank elements. The combination of geodesic curves and asymptotic curves generates a hybrid triangulated network, which offers improved local and global stability compared to conventional lamella structures. The experiments involving local area loading and one-shell asymmetric loading demonstrate the feasibility and reliability of this novel timber gridshell, providing innovative solutions for practical engineering applications in the future. A strong correspondence between the experiments and simulations for all load cases validates the numerical method.

The "inverted dome" behavior of the gridshell is observed for the full-span uniform load. The investigated timber gridshell is optimal for uniformly distributed loads, with a live load capacity of up to 7.0 kN/m^2 (a total load of 392 kN) achievable through simulation. The non-polar array layout arrangement of hybrid asymptotic-geodesic-asymptotic members in the third shell negatively impacts the structural behavior. An ideal polar array layout for member arrangement is expected to obtain a stiffer and stronger structure. The AA-joints function similarly to hinges around the local *y*-axis, and their rotational stiffness around the *y*-axis has minimal impact on the overall structural behavior during normal service periods. Consequently, the configuration of AA-joints does not need to be rigid, which facilitates the design and construction of the timber gridshell. The support condition plays a crucial role in activating shell-like force transfer and ensuring structural stiffness. When the structure's span is large, stresses and displacements due to the self-weight of the structural material become limiting factors for span extension. The maximum span achievable by the structure with a constant overall geometry and mesh configuration is approximately 27.6 m.

In upcoming research, efforts will be made to enhance the span by modifying various parameters, including network and cross-sectional configurations. This improvement may likely be accomplished by augmenting the mesh density, expanding double-lamella spacing, and strengthening continuum couplings between double-lamellas. Moreover, the initial stress generated during construction, which is then mitigated by watering and stress relaxation effects, remains ambiguous within the timber lamellas. Investigating the impact of this residual stress on load-bearing capacity will serve as the subsequent area of exploration.

Future research will focus on enhancing the span by modifying various parameters, including network and cross-sectional configurations. This improvement may be achieved by increasing mesh density, extending double-lamella spacing, and reinforcing continuum couplings between double-lamellas.

CRediT authorship contribution statement

Zongshuai Wan: Writing – review & editing, Writing – original draft, Visualization, Validation, Software, Project administration, Methodology, Investigation, Formal analysis, Data curation, Conceptualization. **Pierluigi D'Acunto:** Writing – review & editing, Visualization, Resources, Funding acquisition. **Eike Schling:** Writing – review & editing, Visualization, Supervision, Resources, Project administration, Funding acquisition.

Declaration of Competing Interest

The authors declare that they have no known competing financial interests or personal relationships that could have appeared to influence the work reported in this paper.

Data availability

Data will be made available on request.

References

[1] Pottmann H. Architectural geometry and fabrication-aware design. Nexus Netw J 2013;15. https://doi.org/10.1007/s00004-013-0149-5.

[2] Pottmann H, Eigensatz M, Vaxman A, Wallner J. Architectural geometry. 64 Comput Graph 2015;47:145. https://doi.org/10.1016/j.cag.2014.11.002.

[3] Huard M, Eigensatz M, Bompas P. Planar panelization with extreme repetition. Adv Archit Geom 2014 2015. https://doi.org/10.1007/978-3-319-11418-7_17.

[4] Happold E, Liddell WI. Timber lattice roof for the mannheim bundesgartenschau. Struct Eng 1975;53.

[5] Chilton J, Tang G. Timber gridshells: Architecture, structure and craft. London and New York. Routledge,; 2016. https://doi.org/10.4324/9781315773872.

[6] Harris R, Romer J, Kelly O, Johnson S. Design and construction of the Downland Gridshell. Build Res Inf 2003;31. https://doi.org/10.1080/0961321032000088007.

[7] Harris R, Roynon J. The Savill garden gridshell design and construction. 10th World Conf Timber Eng 2008;vol. 4:2008.

[8] Bessini J, Lázaro C, Monleón S. A form-finding method based on the geometrically exact rod model for bending-active structures. Eng Struct 2017;152. https://doi.org/10.1016/j.engstruct.2017.09.045.

[9] Pottmann H., Asperl A., Hofer M., Kilian M. Architectural geometry. Bentley Institute Press; 2007.

[10] Pirazzi C, Weinand Y. Geodesic lines on free-form surfaces - Optimized grids for timber rib shells (WCTE) 9th World Conf Timber Eng 2006;vol. 1:2006.

[11] Natterer J, Burger N, Müller A, Natterer J. Holzrippendächer in Brettstapelbauweise - Raumerlebnis durch filigrane Tragwerke. Bautechnik 2000; 77. https://doi.org/10.1002/bate.200006410.

[12] Pottmann H, Huang Q, Deng B, Schiftner A, Kilian M, Guibas L, et al. Geodesic patterns. ACM Trans Graph 2010;29. https://doi.org/10.1145/1833351.1778780.

[13] Soriano E. Low-tech geodesic gridshell: almond pavilion. ArchiDOCT 2017;4.

[14] Finsterwalder S. Mechanische Beziehungen bei der Flächen-Deformation. Teubner: Jahresbericht der Deutschen Mathematiker-Vereinigung; 1897.

[15] Tang C, Kilian M, Bo P, Wallner J, Pottmann H. Analysis and design of curved support structures. Adv Archit Geom 2016;2016.

[16] Jiang C, Wang C, Schling E, Pottmann H, Jiang C, Wang C, et al. Computational design and optimization of quad meshes based on diagonal meshes. Adv Archit Geom 2021.

[17] Schling E., Hitrec D., Schikore J., Barthel R. Design and construction of the asymptotic pavilion. 8th International Conference on Textile Composites and Inflatable Structures - STRUCTURAL MEMBRANES 2017, 2018.

[18] Schikore J, Schling E, Oberbichler T, Bauer AM. Kinetics and design of semi-compliant grid mechanisms. Adv Archit Geom AAG 2021;2020.

[19] Schling E, Wan Z. A geometry-based design approach and structural behaviour for an asymptotic curtain wall system. J Build Eng 2022;52. https://doi.org/10.1016/j.jobe.2022.104432.

[20] Schikore J. Doctoral dissertation. technical university of Munich. Compliant Grids: Theory, Des Realiz 2023.

[21] Wan Z, Schling E. Structural principles of an asymptotic lamella curtain wall. Thin-Walled Struct 2022;180. https://doi.org/10.1016/j.tws.2022.109772.

[22] Wan Z, Schling E. Structural behaviour of an asymptotic curtain wall stiffened with lamella couplings. J Constr Steel Res 2023;207:107938. https://doi.org/10.1016/j.jcsr.2023.107938.

[23] Schling E, Wang H, Hoyer S, Pottmann H. Designing asymptotic geodesic hybrid gridshells. CAD Comput Aided Des 2022;152. https://doi.org/10.1016/j.cad.2022.103378.

[24] Schling E, Wan Z, Wang H, D'Acunto P. Asymptotic Geodesic Hybrid Timber Gridshell. Advances in Architectural Geometry, 2023. De Gruyter,; 2023. p. 97–110. https://doi.org/10.1515/9783111162683-008.

[25] Abaqus. Abaqus Analysis User's Manual. Abaqus 612 2012;1.

[26] British Standards Institution., European Committee for Standardization. DIN EN 338 2016: Structural timber - strength classes. 2016.

[27] Pan Y, Zhang Q, Wang X, Guo R. Research on mechanical model of dovetail joint for Chinese ancient timber structures. Jianzhu Jiegou Xuebao/J Build Struct 2021; 42. https://doi.org/10.14006/j.jzjgxb.2019.0528.

[28] European Committee for Standardization. DIN EN 10088–1:2014 Stainless steels - Part 1: List of stainless steels. Brussels: 2014.

[29] European Committee for Standardization. EN 1993–1-4: Eurocode 3: Design of steel structures-Part 1–4: General rules-Supplementary rules for stainless steels. Design of Structural Elements 2015.

[30] Hong J-P, Barrett D. Three-dimensional finite-element modeling of nailed connections in wood. J Struct Eng 2010;136. https://doi.org/10.1061/(asce) st.1943-541x.0000160.

[31] Hong JP, Barrett JD, Lam F. Three-dimensional finite element analysis of the Japanese traditional post-and-beam connection. J Wood Sci 2011;57. https://doi. org/10.1007/s10086-010-1151-0.

[32] EN 1995–1-1: Eurocode 5: Design of timber structures - Part 1–1: General - Common rules and rules for buildings. 2004.

[33] Long W. Timber Structure Design Handbook. Beijing: China Architecture & Building Press; 2021.

[34] Rubin H. Evaluierung der linearen und nichtlinearen Stabstatik in Theorie und Software. Prüfbeispiele, Fehlerursachen, genaue Theorie. Von G. Lumpe, V. Gensichen. Stahlbau 2014;83. https://doi.org/10.1002/stab.201490107.

[35] https://www.burohappold.com/projects/weald-downland-gridshell/.

[36] Forest Products Laboratory - USDA. Wood Handbook: Wood as an Engineering Material. 2010.

[37] Aondio P. Berechnung von Zylinderschalen aus Holz und Holzwerkstoffen unter Berücksichtigung der Spannungsrelaxation. Technischen Universität München, 2014.

[38] Girardeau-Montaut D. CloudCompare. France: EDF R&D Telecom 2016.

[39] Sandaker B.N., Eggen A.P., Cruvellier M.R. The structural basis of architecture, Third Edition. 2019. https://doi.org/10.4324/9781315624501.

[40] Lienhard J, Knippers J. Considerations on the scaling of bending-active structures. Int J Space Struct 2013;28. https://doi.org/10.1260/0266-3511.28.3-4.137.

[41] EN 1990: Eurocode - Basis of structural design. 2002.

[42] JGJ 7-2010: Technical specification for space frame structures. Beijing: 2010.